Volume 11
Number 22
14 June 2023
Pages 11537–11910

Journal of Materials Chemistry A

Materials for energy and sustainability

rsc.li/materials-a

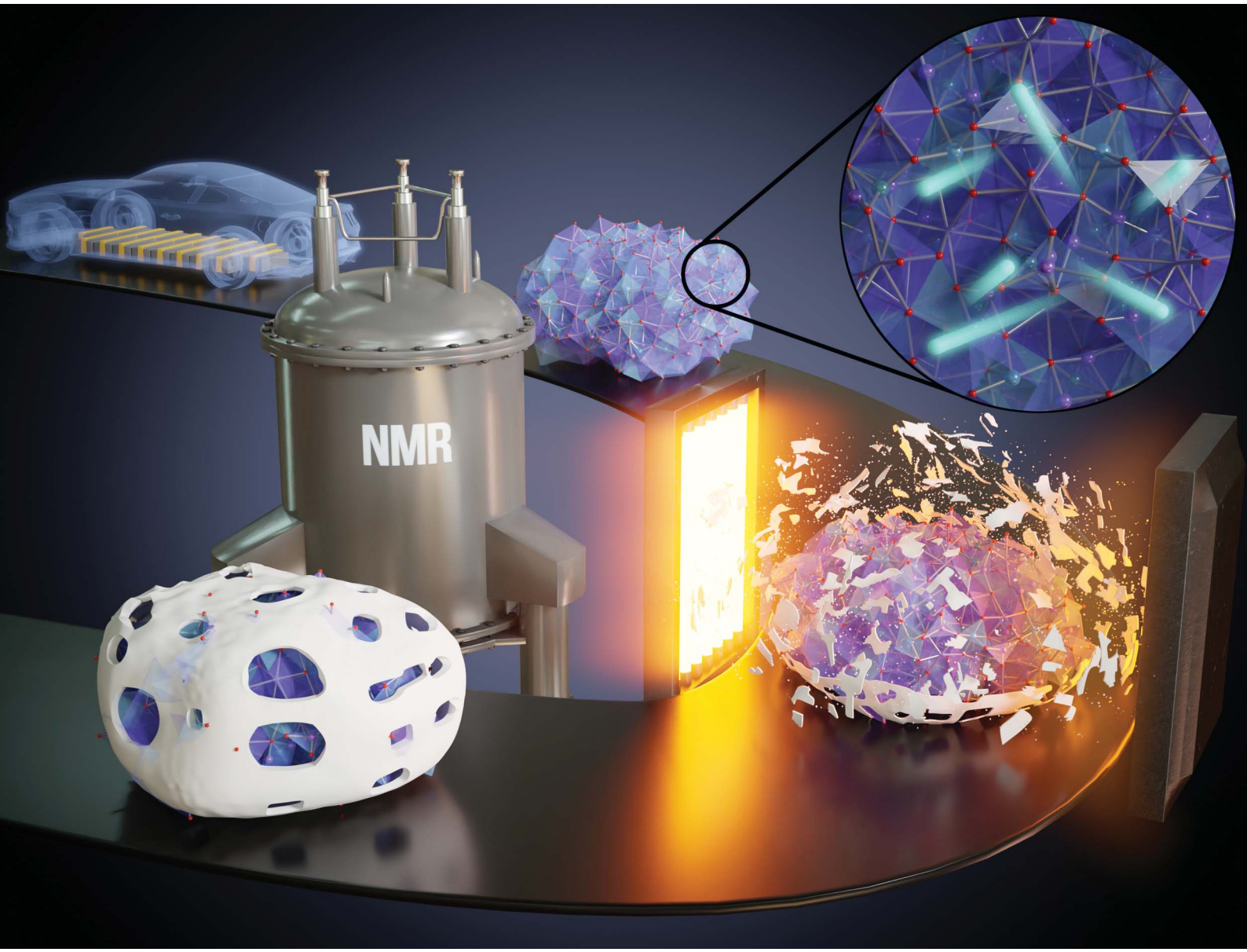

ISSN 2050-7488

ROYAL SOCIETY OF CHEMISTRY

PAPER

Juan Miguel López del Amo *et al.*
Impact of thermal treatment on the Li-ion transport, interfacial properties, and composite preparation of LLZO garnets for solid-state electrolytes

10 YEARS ANNIVERSARY

Journal of Materials Chemistry A

ROYAL SOCIETY OF CHEMISTRY

PAPER

View Article Online
View Journal | View Issue

Check for updates

Cite this: *J. Mater. Chem. A*, 2023, **11**, 11675

Impact of thermal treatment on the Li-ion transport, interfacial properties, and composite preparation of LLZO garnets for solid-state electrolytes†

Pedram Ghorbanzade, [ab] Arianna Pesce, [a] Kerman Gómez,[a] Grazia Accardo, [a] Shanmukaraj Devaraj, [a] Pedro López-Aranguren [a] and Juan Miguel López del Amo *[a]

Received 23rd February 2023
Accepted 7th April 2023

DOI: 10.1039/d3ta01145c

rsc.li/materials-a

Solid state batteries are the next generation of safe energy storage devices offering high energy and power. $Li_7La_3Zr_2O_{12}$ garnets are fast Li-ion conductors and promising electrolytes to be used in solid-state batteries. However, they react with humid air to form LiOH and Li_2CO_3, reducing the ionic conductivity. In this work, the effect of heat treatment on local Li mobility in LLZO and the chemical evolution and phase transitions during the heating are investigated by a combination of solid state NMR, Raman, and XRD diffraction techniques. The results show that the activation energy for Li jumps obtained by variable temperature solid state NMR decreases after heat treatment at 750 °C and the Li dynamics are comparable to those of sintered pellets. Additionally, we show that the pretreatment of powders is an effective approach for obtaining garnet-rich composite electrolytes with better flexibility and garnet-polymer interphases, improving the prospects of this material towards processing.

Introduction

Since the commercialization of Li-ion batteries (LIBs) in 1990, many advances have been made in their performance, offering nowadays high volumetric and gravimetric energy densities as well as long cycle life.[1,2] However, the liquid electrolytes commonly used in LIBs have rather low thermal stability and are flammable.[3,4] Therefore, substituting the liquid electrolyte with a non-flammable solid-state electrolyte has been proposed to increase battery safety.[5] In addition, solid electrolytes could mitigate the growth of Li dendrites, hence allowing the use of Li metal as the negative electrode, increasing considerably the energy density of the cells.[6–8] $Li_7La_3Zr_2O_{12}$ (LLZO) garnets are shown to be a promising choice to be used as solid-state electrolytes, as they offer high bulk Li-ion conductivities (10^{-3} S cm^{-1} at 25 °C) while benefiting from high thermal and electrochemical stabilities.[9]

LLZO exists in three crystallographic phases: (i) high Li^+ conductive cubic, (ii) tetragonal, and (iii) low temperature cubic.[10–12] Due to the presence of vacancies at Li sites and shorter Li–Li distances, the ionic conductivity of the high Li^+ conductive cubic phase is more than two orders of magnitude higher than in the other LLZO phases.[11,13]

One of the main drawbacks of LLZO for practical applications is their air-sensitive nature.[14–16] When exposed to humid air, they undergo a reversible Li^+/H^+ exchange, covering the surface with a layer rich in LiOH, Li_2CO_3, and $Li_{7-x}H_xLa_3Zr_2O_{12}$, with the protonation degree varying along its depth.[14,17] Chemical reactions undergoing at the surface of LLZO from the hydration of the material have been proposed previously[14,15,17] as reported in reactions (1) and (2):

$$Li_7La_3Zr_2O_{12} + xH_2O \rightarrow Li_{7-x}H_xLa_3Zr_2O_{12} + xLiOH \quad (1)$$

$$2LiOH + CO_2 \rightarrow Li_2CO_3 + H_2O \quad (2)$$

In addition to LiOH and Li_2CO_3, other secondary products such as Li_2O or $La_2Zr_2O_7$ can form upon the decomposition of Li_2CO_3 and LLZO respectively.[17,18]

The formed layer has been proved to increase the grain boundary resistance in solid inorganic electrolytes and form a poor interface with Li metal.[19] Therefore, a heat treatment process for the elimination of these surface components was reported in several studies.[15,17,19] For instance, Sharafi *et al.*[19] showed that heat treatment of the LLZO garnet at 500 °C can remove the surface layer and improve the Li wetting, while Li *et al.*[20] proposed reacting garnet pellets with carbon at 700 °C to completely remove Li_2CO_3. Other approaches such as co-sintering,[21] flame vapor deposition[22] and chemical treatment[23]

[a]*Centre for Cooperative Research on Alternative Energies (CIC energiGUNE), Basque Research and Technology Alliance (BRTA), Alava Technology Park, Albert Einstein 48, Vitoria-Gasteiz 01510, Spain. E-mail: jmlopez@cicenergigune.com*

[b]*University of Basque Country (UPV/EHU), Barrio Sarriena, s/n, Leioa 48940, Spain*

† Electronic supplementary information (ESI) available. See DOI: https://doi.org/10.1039/d3ta01145c

were also successful in eliminating the carbonate layer and modifying the interface. Although the heat treatment is proven to be significant to clean the garnet surface and form a better interface with the Li metal,[15,17,19] its effect on Li^+ dynamics within the garnet structure is less investigated. Using solid state NMR spectroscopy, we study the impact of heat treatment on the Li^+ mobility inside the garnet structure and the crystallographic phase transitions undergoing at different temperatures. Moreover, the application of this heat processing as a pretreatment stage in either sintering at high temperature and processing of a composite polymer electrolyte is investigated.

Among several LLZO compositions with different doping elements or contents, $Li_{6.75}La_3Zr_{1.75}Nb_{0.25}O_{12}$ was selected for this study, as this Nb doping content has been shown to be enough to stabilize the cubic structure after sintering, while keeping the Nb dopant at a minimum.[24] Considering that Nb can be reduced in contact with Li metal, negatively affecting the cell performance,[25,26] a low amount of Nb doping is more suitable for practical applications.

Experimental section

Commercially available $Li_{6.75}La_3Zr_{1.75}Nb_{0.25}O_{12}$ (T-Pristine) provided by Toshima Manufacturing Co. was heat treated at 350 °C, 550 °C, and 750 °C for 12 hours in a synthetic air (SA) atmosphere applying a heating rate of 3 °C min^{-1}. These samples are denoted as T-350, T-550 and T-750 respectively. To avoid moisture exposure, the heat treatment was conducted in a high-temperature furnace connected to a glovebox ($O_2 \leq$ 0.1 ppm, $H_2O \leq$ 0.1 ppm), where the sample handling was performed.

Sintered pellets were prepared by applying 1.5 ton pressure on T-Pristine and T-750 in a die with a diameter of 10 mm. The pellets were sintered for 6 hours at 1200 °C in SA, while being covered with mother powder to avoid lithium evaporation at high temperatures. After polishing, Li symmetrical Swagelok cells were assembled for electrochemical tests.

Composite polymer electrolytes containing 90 wt% garnet were prepared by dissolving the Lithium bis(trifluoromethanesulfonyl)imide (LiTFSI) salt (Solvionic) and poly(ethylene oxide) (PEO, 5×10^6 g mol^{-1}, Sigma Aldrich) in acetonitrile (EO:Li = 20). The solution was ball-milled together with the LLZO garnet in a Pulverisette 7 for proper mixing and was later cast in PTFE evaporation dishes. The membranes were dried for 12 hours in a vacuum oven at 50 °C to ensure solvent evaporation.

Commercial Al-doped LLZO ($Li_{6.24}La_3Zr_2Al_{0.24}O_{11.98}$) was purchased from NEI Corporation and was heat treated at 750 °C following the same procedure as for Nb-LLZO.

Thermogravimetric analysis (TGA) was performed with a TG209 F1 Libra Netzsch in SA with a heating rate of 10 °C min^{-1} in the temperature range of 30 to 1000 °C.

The pristine and heat treated garnets were characterized by powder X-ray diffraction (PXRD) using a Bruker D8 Discover X-ray diffractometer with $\lambda_{Cu\ K\alpha} = 1.54056$ Å in the range of $2\theta =$ 10° to 80° and a step-size of 0.02°.

Raman spectra were recorded at room temperature in the range of 100–1500 cm^{-1} using a Renishaw inVia confocal Raman microscope in a custom air-tight sample holder. The laser wavelength (532 nm^{-1}), number of accumulations (100) and exposure time (5 s) were kept constant for all measurements.

Magic Angle Spinning Nuclear Magnetic Resonance (MAS NMR) spectroscopy was performed on pristine and heat treated garnet powders using a Bruker Avance III 500 spectrometer equipped with a 2.5 mm probe. The MAS frequency was set to 20 kHz unless otherwise specified. ^{7}Li and ^{1}H chemical shifts were referenced to 0.1 M LiCl solution and bulk water respectively. ^{7}Li 1D experiments were performed using single excitation pulses (2.4 μs) and relaxation delays of 1200 s to ensure full relaxation of the nuclei. ^{1}H 1D spectra were recorded using Hahn Echo experiments with a $\pi/2$ pulse (1.9 μs) followed by a π pulse (3.8 μs) and a recycle delay of 3 s. ^{7}Li relaxation times were obtained from saturation-recovery experiments considering single or multiple exponential functions as specified in each case. ^{1}H–^{1}H EXchange SpectroscopY (EXSY) correlations were obtained using standard three $\pi/2$ pulse experiments for 1.9 μs. ^{1}H–^{7}Li HETeronuclear CORrelation (HETCOR) experiments were performed using a Cross Polarization (CP) ^{1}H–^{7}Li magnetization transfer step of 1 ms. Variable temperature experiments were conducted in the temperature range of −110 to 100 °C in a static probe, and the ^{7}Li 1D experiments were performed using single scans.

Electrochemical Impedance Spectroscopy (EIS) of the sintered pellets was conducted using a Solartron 1260 FRA module, with AC in a frequency range of 32 MHz to 1 Hz and a bias voltage of 50 mV in the temperature range of 30 to 80 °C with intervals of 10 °C. The spectra were fitted with an equivalent circuit containing one resistance element for the external resistance in series with three R//CPE blocks.

The morphology of solid electrolytes was characterized with a Scanning Electron Microscope (SEM Quanta FEG 250) using a backscattered electron detector (BSD) with an accelerating voltage of 10 kV.

Results and discussion

The mass evolution of the pristine garnet (T-Pristine) upon increasing temperatures was revealed by TGA. The TG and its derivative (Fig. 1) show a rather complex behavior with different thermal decomposition events, well highlighted by the endothermic peaks. Four main regions can be identified in this experiment. A low amount of weight loss (~4%) occurred below 300 °C. This step is ascribed to the evaporation of H_2O molecules adsorbed on the surface. In the second and third regions between 300–550 °C and 550–730 °C, the total weight losses are approximately 11% and they are recognized with the emission of CO_2 and water.[27] Above 730 °C, the weight losses are almost completed. According to this behavior, 350 °C, 550 °C and 750 °C were selected as different stages for the detailed characterization of the heat treatment.

The garnets heated at different temperatures were analysed by X-ray diffraction, Raman, and solid state NMR to observe

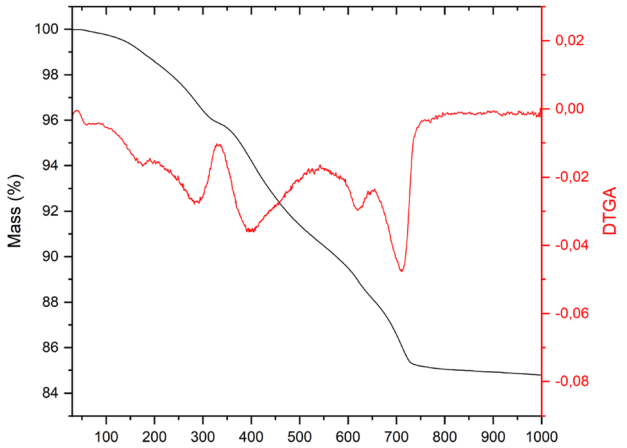

Fig. 1 TGA and DTGA curves of T-Pristine.

possible phase transitions and detect the formation of new phases such as pyrochlore at high temperatures. The XRD patterns presented in Fig. 2 show splitting of the diffraction peaks for all the heat treated samples. As previously reported,[18,28] this phenomenon indicates the coexistence of tetragonal and cubic phases of the garnet. The XRD pattern also shows an extra peak at $2\theta = 28.4°$ for T-550. This peak is characteristic of $La_2Zr_2O_7$ pyrochlore, formed at such a temperature according to reaction (3) and reported by Geng *et al.*[29]

$$Li_7La_3Zr_2O_{12} \rightarrow La_2Zr_2O_7 + Li_7LaO_5 \quad (3)$$

By increasing the heat treatment temperature to 750 °C, the same reaction takes place in the reverse direction and LLZO is formed,[13] in agreement with the disappearance of the pyrochlore peak in the XRD pattern of T-750 (Fig. 2). Since the secondary phases cause the heat treated samples to not be perfectly crystalline, and since X-ray powder diffraction cannot precisely differentiate the low temperature cubic phase from the highly Li^+ conductive cubic phase,[18] Raman spectroscopy was used both to identify the crystallographic phases and detect the presence of lithium carbonates on the outermost surface. The Raman analysis for the mentioned samples is reported in Fig. 3. The high-frequency region of the spectra between 550 cm^{-1} and 800 cm^{-1} shows the vibrational stretching mode of ZrO_6 and NbO_6 at 645 cm^{-1} and 720 cm^{-1} respectively.[30–32] The signals in the intermediate-energy range of 300–550 cm^{-1} correspond to the bending modes of the octahedral and tetrahedral units, while the low-energy region below 300 cm^{-1} consists of translational modes of mobile cations.[31] The Raman spectra of Li_2CO_3 typically display an intense band at around 1090 cm^{-1} which is assigned to its symmetric stretching vibration. This characteristic signal is clearly observed in the Raman spectra of the samples T-Pristine, T-350 and T-550, indicating the insufficiency of such temperatures for the complete removal of carbonates. The Raman spectra of the cubic garnet contain a smaller number of peaks than the tetragonal phase, due to its higher symmetry. In addition, the higher disorder nature of Li^+ ions in the cubic phase results in broader and more overlapping bands.[18,31] As can be observed in the Raman spectrum of T-Pristine, the stretching vibrations of ZrO_6 in the low temperature cubic phase show a noticeable shift to higher wavenumbers, which makes it easy to identify. The Raman spectrum of the tetragonal phase shows a strong band at 248 cm^{-1} and doublets at 108 and 122 cm^{-1}, while the highly Li conductive cubic phase display a single medium intense band at 122 cm^{-1} with a shoulder at 108 cm^{-1}.[18] Using this information, the crystallographic phases in each sample were identified, although the presence of multiple overlapping peaks in the range of 200–400 cm^{-1} and strong fluorescence in T-350 makes it difficult to completely resolve the spectra and quantify the

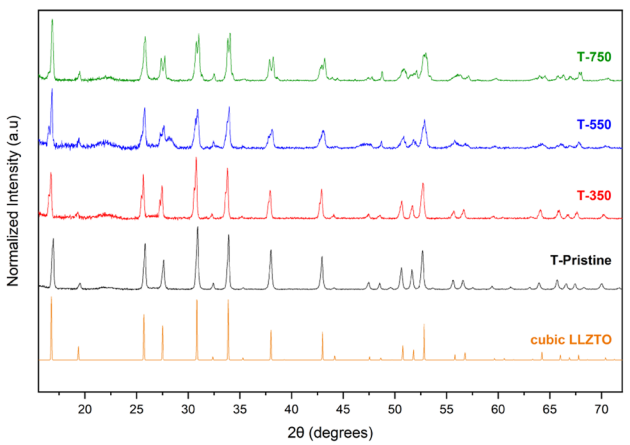

Fig. 2 PXRD patterns of T-Pristine, T-350, T-550, T-750 and reference cubic LLZTO (PDF-01-080-6318).

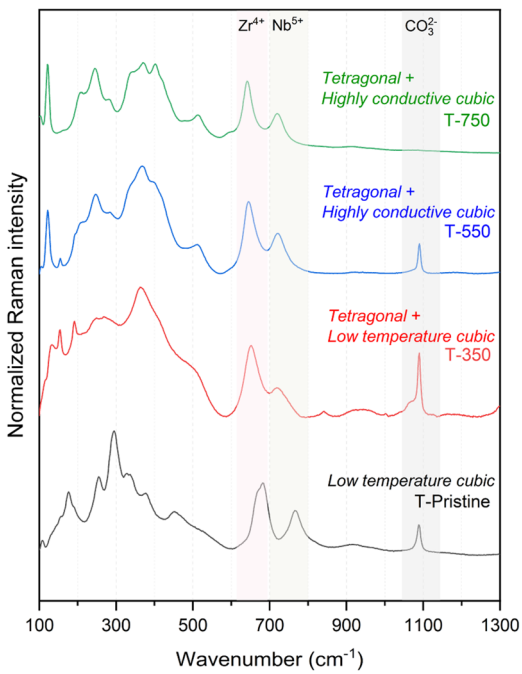

Fig. 3 Raman spectra of T-Pristine, T-350, T-550 and T-750 and their corresponding crystallographic phases.

phases. Fig. 3 shows the identified phases for each sample and the complete removal of Li_2CO_3 after heat treating at 750 °C. While T-Pristine shows only a low temperature cubic phase, in all the heat treated samples, the tetragonal phase is present, coexisting with the low temperature cubic phase in T-350, and with the highly conductive cubic phase in T-550 and T-750.

Solid state NMR experiments were conducted on the pristine and heat treated samples to further determine the impact of temperature on the composition and to characterize local Li^+ dynamics. The ^1H NMR spectrum of T-Pristine is characterized by three main signals (Fig. 4a) appearing at −1.6 ppm, 0.9 ppm, and 3.9 ppm. The signal at −1.6 ppm can be easily ascribed to LiOH in agreement with values previously observed for this compound formed as a secondary product of garnet protonation.[33–37] The signal at 3.9 ppm was also previously observed upon LLZO protonation and is ascribed to protons inside the garnet structure.[33–35] The ^1H–^7Li HETCOR correlation experiment performed for this sample (Fig. 4c) clearly shows the strong correlation of ^1H signals at −1.6 and 3.9 with ^7Li, in agreement with protons in LiOH and protons coexisting with lithium in $Li_{7-x}H_xLa_3Zr_2O_{12}$. The signal at 0.9 ppm, which was previously observed but not specifically assigned,[33,35] is relatively sharp in the ^1H spectrum, but does not show a clear correlation with Li in the CP-based spectrum of Fig. 4b. These proton signals could be attributed to the protons of the water molecules adsorbed at the surface of LLZO or included at its surface defects, forming LLZO·H_2O through reaction (4).[12]

$$Li_{7-x}H_xLa_3Zr_2O_{12} + xH_2O \rightarrow Li_{7-x}H_xLa_3Zr_2O_{12}\cdot nH_2O \quad (4)$$

To further explore the nature and disposition of the protonated phases ascribed to the observed proton signals, ^1H–^1H EXSY homonuclear correlations were determined. This experiment was performed for T-Pristine with a mixing time of 128 ms. The resulting spectrum shown in Fig. 4c is characterized by a diagonal with autocorrelation signals observed in the 1D spectrum and off-diagonal correlations between signals at 3.9 and 0.9 ppm as well as between signals at −1.6 and 0.9 ppm. Since signals at 3.9 and −1.6 ppm are assigned to protons inside the garnet structure and LiOH at the surface of the particles respectively, the protons observed at 0.9 ppm should be placed in close vicinity of both phases. This is in agreement with water molecules adsorbed at the surface of LLZO. The narrower character of this signal at 0.9 ppm is also in agreement with the faster local mobility expected for a water molecule. Additional ^1H–^1H EXSY NMR experiments performed with very short (0.1 ms) and long (256 ms) mixing times presented in Fig. S1,† indicate that off-diagonal correlations are caused by chemical exchange.

The ^1H and ^7Li NMR spectra as well as ^7Li T_1 times of the pristine garnet, T-350, T-550, and T-750 (Fig. 5a–c respectively) were recorded and compared in order to observe the effect of the heat treatment on the Li local mobilities and states of protonation. From the inspection of the ^1H NMR signal

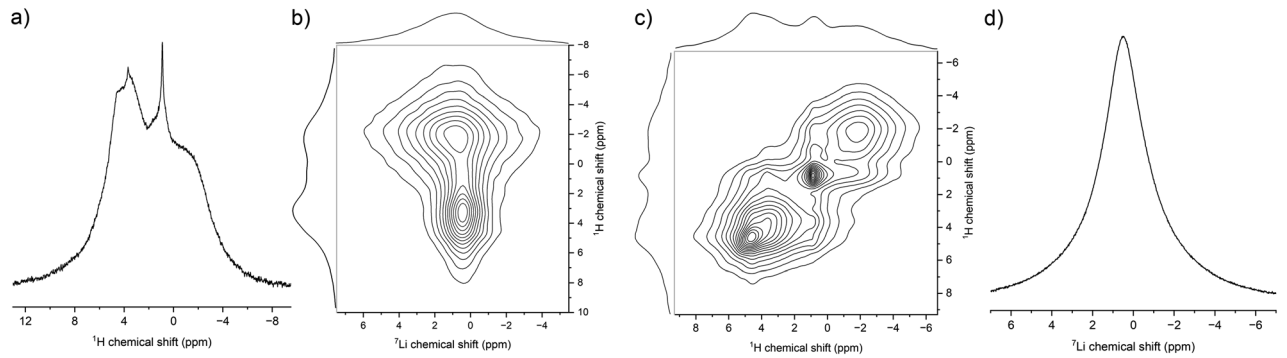

Fig. 4 (a) ^1H NMR spectrum, (b) ^7Li–^1H 2D heteronuclear correlation, (c) ^1H–^1H 2D correlation with a mixing time of 128 ms and (d) ^7Li NMR spectrum of T-Pristine.

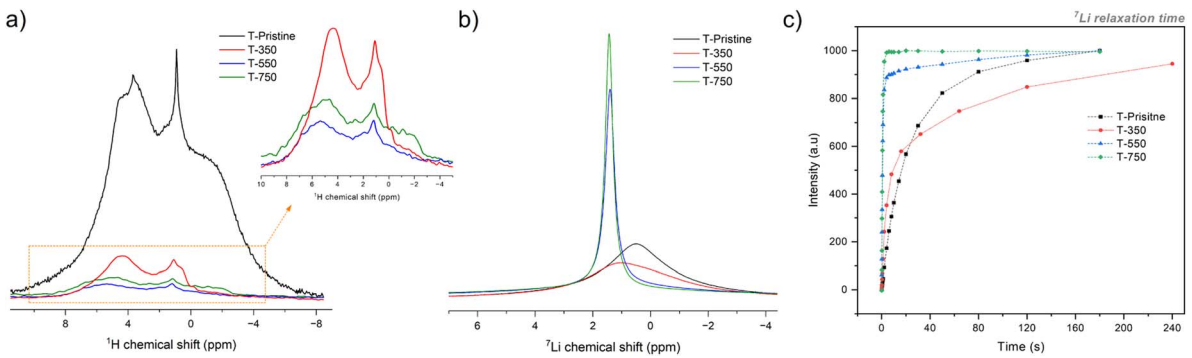

Fig. 5 (a) ^1H NMR spectra and (b) ^7Li NMR spectra and (c) ^7Li saturation recovery experiment of T-Pristine, T-350, T-550 and T-750.

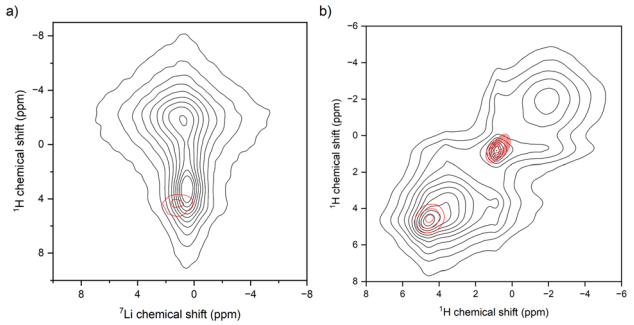

Fig. 6 (a) ^{1}H–^{7}Li heteronuclear experiment and (b) ^{1}H–^{1}H homonuclear experiment for T-Pristine (black) and T-350 (red).

evolution upon heat treatment (Fig. 5a), a significant reduction of intensity of the proton signal is observed already for the sample T-350. The reduction of proton intensity observed involves the three signals present in the spectrum of T-Pristine, suggesting the removal of water molecules from LLZO·H_2O, protons from inside the structure, and LiOH from the garnet surface through reactions (5)–(7) respectively.

$$Li_{7-x}H_xLa_3Zr_2O_{12}\cdot nH_2O \rightarrow Li_{7-x}H_xLa_3Zr_2O_{12} + xH_2O \quad (5)$$

$$Li_{7-x}H_xLa_3Zr_2O_{12} \rightarrow Li_{7-x}La_3Zr_2O_{12-\frac{x}{2}} + \frac{x}{2}H_2O \quad (6)$$

$$Li_{7-x}H_xLa_3Zr_2O_{12} + xLiOH \rightarrow Li_7La_3Zr_2O_{12} + xH_2O \quad (7)$$

Comparing the ^{1}H–^{1}H and ^{7}Li–^{1}H correlations in T-Pristine and T-350 (Fig. 6a and b), we can observe that LiOH is completely removed, and only a small proton population remains. As a result, the signal intensities are low, and no magnetization transfer can be observed between protons inside the garnet.

As can be observed in Fig. 5b, the ^{7}Li signal in both T-Pristine and T-350 is broad, although it is clear that at least for T-350, the signal has more than one component, probably due to the presence of more than one Li compound. This is in agreement with the clear carbonate band in the Raman spectra (Fig. 3), as well as ^{7}Li T_1 measurements (Fig. 5c and Table S1†), in which the build-up curves of both T-Pristine and T-350 can be fitted only by a double exponential term, indicating the presence of two Li reservoirs with considerably different relaxation times. In general, the presence of fast Li^+ dynamics results in shorter relaxation times in highly conductive ceramics as compared to the long relaxation times typically observed for non-conductive salts like Li_2CO_3. By elimination of the protons inside the garnet structure, the Li T_1 relaxation time decreases from 17 s to 3.9 s (Table S1†).

When the heat treatment temperature was increased to 550 °C and 750 °C, the ^{1}H signals are further reduced, indicating additional proton elimination through reaction (6). No signals were observed for the heteronuclear ^{1}H–^{7}Li and homonuclear ^{1}H–^{1}H NMR correlations conducted on both samples T-550 and T-750. This result suggests complete elimination of protons in the sample and that the remaining proton signals observed in Fig. 5a are due to background proton signals from the probe or the rotor and therefore external to the sample.

In general, the linewidth (FWHM) of ^{7}Li NMR signals is directly related to ion dynamics, as faster ion motions can effectively average out the anisotropic interactions present in the solid state,[38,39] reducing the observed linewidths. Fig. 5b shows a significant reduction of the linewidth of ^{7}Li NMR resonances from 691 Hz to 79 Hz after heat treatment at 550 °C, implying faster local dynamics for Li^+ in the T-550 sample. This change can be explained by a phase transition from tetragonal to highly conductive cubic, as well as by partial removal of the rigid lithium carbonates (reaction (8)) as shown previously by Raman spectroscopy in Fig. 3.

$$Li_{7-x}La_3Zr_2O_{12-\frac{x}{2}} + \frac{x}{2}Li_2CO_3 \rightarrow Li_7La_3Zr_2O_{12} + \frac{x}{2}CO_2 \quad (8)$$

By further increasing the heat treatment temperature to 750 °C, a further narrowing of the ^{7}Li NMR signal is observed from 79 Hz to 64 Hz. In addition, the build-up curve of the saturation recovery experiment (Fig. 5c and Table S1†) can be fitted by a single exponential term only after heat treating at 750 °C, which indicates complete removal of Li_2CO_3 and is consistent with our results from Raman measurements (Fig. 3). It is noteworthy that according to reaction (8) and based on our ICP results (Table S2†), the Li from the carbonate is not lost and rather returns to the garnet structure after the Li_2CO_3 decomposition. Furthermore, reaction (8) implies the recovery of the oxygen vacancies that could be generated at the LLZO surface by the proton elimination through water evaporation described in reaction (6).

To perform a detailed characterization of the Li dynamics in the pristine and T-750 heat treated samples, variable temperature ^{7}Li Linewidth (LW) evolutions were measured and compared with those of sintered pellets. The transition from broad gaussian NMR signals observed at the rigid lattice (low temperatures) to narrow Lorentzian peaks at thermally activated states is clearly observed in all samples except in T-Pristine where the high temperatures required for fast Li^+ dynamics could not be experimentally reached (Fig. 7a). The motional narrowing (MN) curves (Fig. 7a) show that unlike T-Pristine, T-750 has a behaviour very similar to the sintered pellets. The resulting temperature-dependance of the ^{7}Li LW were fitted considering a Boltzmann function (eqn (9)) to obtain the inflection point and linewidth of the rigid lattice for each sample.

$$y = \frac{A_1 - A_2}{1 + e^{(x-x_0)/dx}} + A_2 \quad (9)$$

Jump rates (at T_{ip}) and the activation energy of motional narrowing (E_a^{MN}) of each sample were calculated through eqn (10) (ref. [40]) and (11) (ref. [41] and [42]) respectively and are presented in Table 1.

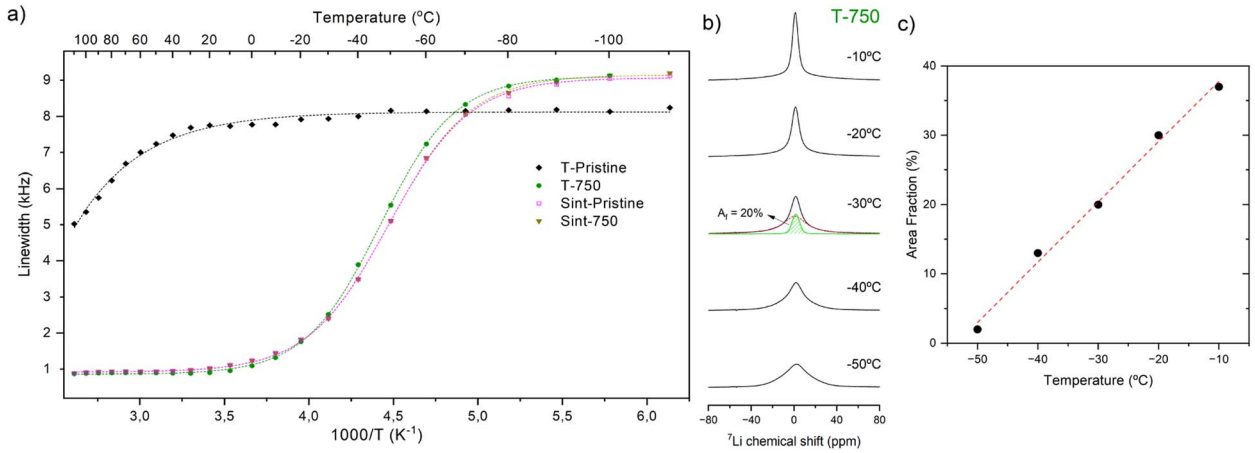

Fig. 7 (a) Temperature dependency of the ^{7}Li linewidth for T-Pristine, T-750, Sint-Pristine, and Sint-750. Dashed lines indicate the fit with the Boltzmann equation. (b) ^{7}Li NMR spectra of T-750 at −50 °C to −10 °C, and deconvolution of the spectrum at −30 °C. (c) Temperature dependency of the area fractions of the narrow components obtained from the deconvolution of spectra with Gaussian and Lorentzian functions.

Table 1 Temperature of the inflection point, activation energy of motional narrowing and the jump rates calculated from the variable temperature ^{7}Li LW analysis shown in Fig. 7a

Sample	T_{ip} (°C)	E_a^{MN} (eV)	τ_{MN}^{-1} (kHz)
T-Pristine	+116	0.49[a]	51.2
T-750	−47	0.30	58.3
Sint-Pristine	−49	0.28	56.9
Sint-750	−49	0.28	57.5

[a] Calculated from eqn (11).

$$\tau_{MN}^{-1} = 2\pi \cdot \omega_{RL} \quad (10)$$

$$\omega(T) = \omega_{RL}\left[1 + \left(\frac{\omega_{RL}}{B} - 1\right)\exp\left(\frac{-E_a^{MN}}{K_B T}\right)\right]^{-1} + D \quad (11)$$

where ω_{RL} is the ^{7}Li linewidth in the rigid lattice, K_B is the Boltzmann constant and D is a line-broadening constant to take the temperature-independent effects such as magnetic field inhomogeneity into account. Eqn (11) which assumes a similar temperature dependency in the fraction of vacancies and the fraction of thermally activated ions is uninfluenced by the possible distribution of relaxation times in the system and therefore can be applied in a wide range of temperature.[41]

Since the high temperature part of the curve could not be achieved for T-Pristine, its activation energy is roughly estimated by using eqn (12) known as the Waugh–Fedin[43] equation.

$$E_a^{WF} = 1.617 \times 10^{-3} \cdot T_{onset} \quad (12)$$

where T_{onset} is the temperature in which the motional narrowing begins, and it is calculated by fitting the tangential lines in the MN curve.

The E_a^{MN} from solid state NMR takes both nonlocalized (long-range ion motions) and localized (dipolar relaxations) conduction into account and therefore is lower than the E_a obtained by EIS. In fact, a thorough calculation of E_a by solid state NMR would require additional T_1, $T_{1\rho}$ and T_2 relaxation time measurements, as well as impedance spectra recorded in a wide temperature and frequency range, which is out of the scope of this study.[44–48]

However, the E_a^{MN} values of T-750, Sint-Pristine and Sint-750 are noticeably lower than that of T-Pristine and are similar to what Buschmann *et al.*[49] reported for highly conductive cubic LLZO with Al doping. At low temperatures, the ^{7}Li NMR spectra of T-750 seem to be composed of 2 overlapping signals, showing different dynamics. Therefore, the spectra were deconvoluted considering Gaussian and Lorentzian functions. The area fraction (A_f) of the narrow component calculated in the range of −50 to −10 °C (Fig. 7b) indicates the fraction of Li ions with fast jump rates (10^4 s^{-1}). Fig. 7c shows that the A_f linearly increases upon heating, and already at −10 °C, about 40% of the Li ions are subject to fast dynamics on the NMR timescale. This further confirms our previous conclusion from ^{7}Li T_1 relaxation time measurements that the heat treatment is not only surface-related, but rather affects the dynamics of the Li atoms in the bulk of the garnet.

The effect of LiOH and Li_2CO_3 removal on the pellet's relative density and its ionic conductivity was investigated by preparing sintered pellets using T-Pristine and T-750 as starting materials. These pellets, referred to as Sint-Pristine and Sint-750 respectively, showed no differences in relative densities (92% in both cases), and very similar activation energies, presented in Fig. 7a and Table 1. The bulk ionic conductivities were calculated using eqn (13), where A is the surface area and ρ is the sample thickness.

$$\sigma = \rho/RA \quad (13)$$

Furthermore, the activation energy from ionic conductivities was obtained through the following Arrhenius equation.

Table 2 Bulk ionic conductivity and activation energy of Sint-Pristine and Sint-750 at 25 and 70 °C obtained by using eqn (13) and (14)

Sample	$\sigma_{25\ °C}$ (S cm^{-1})	$\sigma_{70\ °C}$ (S cm^{-1})	E_a (eV)
Sint-Pristine	3.7×10^{-4}	3.5×10^{-3}	0.43
Sint-750	5.1×10^{-4}	4.2×10^{-3}	0.43

$$\sigma = \sigma_0 e^{\left(-\frac{E_a}{K_B T}\right)} \quad (14)$$

Both Sint-Pristine and Sint-750 show identical activation energies (0.43 eV) and comparable bulk ionic conductivities at 25 and 70 °C, as presented in Table 2 and Fig. S2.†

We can therefore conclude that heat treating the powder prior to pelletizing and sintering shows no considerable improvement in electrochemical performance. This result demonstrates that the high temperatures used during the sintering processing directly promotes proton, hydroxide, and carbonate removal. However, based on the significant increase of local Li^+ mobility observed from the pristine to heat treated powder, shown in Fig. 7a, heat treating LLZO at 750 °C is expected to have a strong influence in cases in which a sintering step is not performed, as for composite electrolytes or cold-sintered pellets in which ion transport is highly sensitive to the interfacial properties of grains. To assess the possible impact of the heat treatment on the Li ion transport at the bulk and the outermost surface of LLZO grains, T-Pristine and T-750 garnets were added to the PEO-LiTFSI mixture to prepare garnet-rich solid composite electrolytes (90 wt% LLZO). The membranes were cast in PTFE dishes and carefully removed after drying in a vacuum oven. Although the sample preparation was the same (as detailed in the Experimental section), the membranes show clearly different mechanical properties as shown in Fig. 8a and c. While the composite made with T-Pristine is highly fragile and non-self-standing, the one containing T-750 has high integrity and is self-standing and flexible.

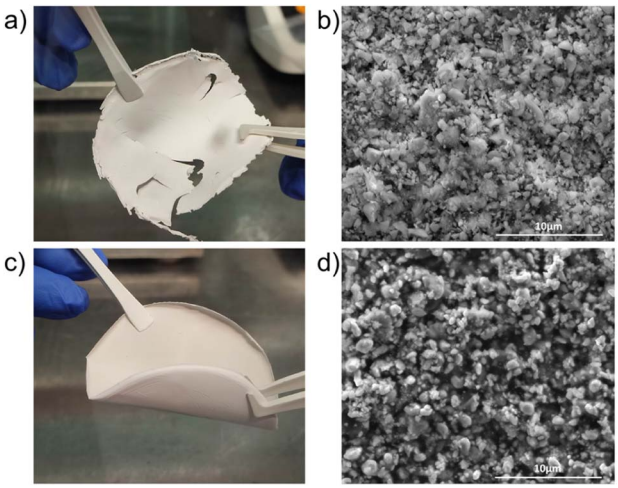

Fig. 8 Photo and SEM micrographs of garnet-rich composite polymer electrolytes containing 90 wt% (a and b) T-Pristine and (c and d) T-750.

The SEM images (Fig. 8b and d) demonstrate that such better mechanical properties could be related to the garnet–polymer interphase. In the composite made of T-750, the garnet particles are uniformly coated with the polymer matrix, whereas in the composite with T-Pristine, many garnet particles are not covered by PEO, which could be attributed to a weak garnet–polymer interaction as a result of the presence of surface group impurities, causing a phase segregation and thus leading to low mechanical properties.

Despite the non-self-standing nature of the composite with T-Pristine, the impedance spectra of these membranes were recorded (Fig. S3†) and the ionic conductivities obtained were 4.3×10^{-6} and 1.6×10^{-5} S cm^{-1} at 70 °C for composites with T-Pristine and T-750 respectively. The higher ionic conductivity of the latter can be attributed to its more homogenous morphology and better PEO–LLZO interface. The low ionic conductivity of garnet-rich composites is not unprecedented and has been previously reported and explained.[50,51] Detailed characterization of the garnet-rich composites and determining their Li-ion pathways are out of the scope of this article and therefore will be the subject of our future work.

It is well known that different dopants and concentrations have an important effect on the Li conductivities of LLZO,[24,30] although it has also been reported that the protonation and formation of LiOH and carbonates are present in garnets regardless of the dopant used.[14,17] The impact of heating on the chemical and thermodynamic processes reported here for a Nb sample are therefore expected to be dopant-independent as mainly surface effects are involved. However, to confirm this hypothesis, additional NMR experiments were performed on commercial Al-doped LLZO. Fig. S4† clearly shows the LiOH formed on the Al-LLZO surface, the adsorbed water molecules and LLZO protonation through a H^+/Li exchange reaction. The comparison of the ^{1}H NMR spectra before and after the heat treatment at 750 °C (Fig. S5†) indicates the total removal of LiOH and water molecules at the surface, and a significant reduction of protons inside the LLZO structure. The considerable reduction of the 7Li T_1 relaxation times upon heat treatment shown in Fig. S6† is attributed to the LiOH and Li_2CO_3 decomposition as well as to the increased Li dynamics upon garnet deprotonation. This confirms that heat treatment at 750 °C is sufficient for complete removal of protons and secondary phases on the Al-LLZO surface. Moreover, like for Nb-LLZO, the heat treatment has a strong impact on the ^{7}Li NMR linewidths, decreasing from 607 to 305 Hz upon heating at 750 °C in agreement with faster local Li dynamics (Fig. S7†).

Concluding remarks

In this work, the impact of heat treatment on the LLZO structure, the secondary products present on its surface, and the Li dynamics inside the garnet was investigated. The characterization of the pristine garnet shows a significant degree of LLZO protonation as well as the presence of water, LiOH and carbonates at the surface. Heat treatment at 350 °C was found

effective to completely eliminate the LiOH at the surface and reduce the number of protons inside the LLZO structure and water at the surface. However, it doesn't suffice to remove carbonates and cause the phase transition to a highly Li conductive cubic phase. Total elimination of carbonates is achieved only after heat treating at 750 °C. Multiple phase transitions from a low temperature cubic phase to a tetragonal phase and later to a highly conductive cubic phase are involved in this process and together with Li_2CO_3 removal are responsible for a significant increase in the local Li mobility inside the garnet structure.

In the second part of this work, the impact of heat treatment at 750 °C as a pre-treatment step in the preparation of sintered pellets was studied. It was observed that pre-treatment of LLZO before sintering is not effective and has no big impact on the Li dynamics and ionic conductivities of sintered pellets. However, since the local mobility of the garnet after heat treatment at 750 °C is alike the sintered pellets and the secondary phases at the surface are removed, we expect this heat-treatment to greatly enhance the ionic conductivity of LLZO in other systems such as ceramic-polymer composite electrolytes in which garnet fillers are not sintered. This improvement could be achieved both by faster Li motion in the bulk of LLZO and by better processability of the garnet-rich composite solid electrolytes. These composite electrolytes will be thoroughly investigated in our future work.

Considering the similar observations on the impact of heat treatment on the interfacial and Li transport properties in Nb and Al-doped LLZO, we believe that the general conclusion of this work could be applied to LLZO garnets, regardless of their doping composition.

Author contributions

PG: investigation, formal analysis, writing-original draft, and writing-review & editing. AP: investigation and writing-review & editing. KG: investigation. GA, PL, and DS: writing-review & editing. JL: investigation, supervision, and writing-review & editing.

Conflicts of interest

There are no conflicts to declare.

Acknowledgements

P. G. as a part of the DESTINY PhD programme acknowledges funding from the European Union's Horizon 2020 research and innovation programme under the Marie Skłodowska-Curie Actions COFUND – Grant Agreement No: 945357. This work was supported by the "Ministerio de Ciencia e Innovación/ Agencia Estatal de Investigación", under the project grant TED2021-129663B-C52.

Notes and references

1 J.-M. Tarascon and M. Armand, *Nature*, 2001, **414**, 359–367.
2 B. Scrosati and J. Garche, *J. Power Sources*, 2010, **195**, 2419–2430.
3 M. Forsyth, L. Porcarelli, X. Wang, N. Goujon and D. Mecerreyes, *Acc. Chem. Res.*, 2019, **52**, 686–694.
4 M. Armand and J.-M. Tarascon, *Nature*, 2008, **451**, 652–657.
5 T. Famprikis, P. Canepa, J. A. Dawson, M. S. Islam and C. Masquelier, *Nat. Mater.*, 2019, **18**, 1278–1291.
6 Q. Zhao, S. Stalin, C. Z. Zhao and L. A. Archer, *Nat. Rev. Mater.*, 2020, **5**, 229–252.
7 Y. Zheng, Y. Yao, J. Ou, M. Li, D. Luo, H. Dou, Z. Li, K. Amine, A. Yu and Z. Chen, *Chem. Soc. Rev.*, 2020, **49**, 8790–8839.
8 J. Li, C. Ma, M. Chi, C. Liang and N. J. Dudney, *Adv. Energy Mater.*, 2015, **5**, 1401408.
9 V. Thangadurai, S. Narayanan and D. Pinzaru, *Chem. Soc. Rev.*, 2014, **43**, 4714–4727.
10 J. Awaka, A. Takashima, K. Kataoka, N. Kijima, Y. Idemoto and J. Akimoto, *Chem. Lett.*, 2011, **40**, 60–62.
11 S. Toda, K. Ishiguro, Y. Shimonishi, A. Hirano, Y. Takeda, O. Yamamoto and N. Imanishi, *Solid State Ionics*, 2013, **233**, 102–106.
12 G. Larraz, A. Orera and M. L. Sanjuán, *J. Mater. Chem. A*, 2013, **1**, 11419–11428.
13 C. Deviannapoorani, S. Ramakumar, N. Janani and R. Murugan, *Solid State Ionics*, 2015, **283**, 123–130.
14 J. Leng, H. Wang, H. Liang, Z. Xiao, S. Wang, Z. Zhang and Z. Tang, *ACS Appl. Energy Mater.*, 2022, **5**, 5108–5116.
15 H. Yamada, T. Ito, S. P. Kammampata and V. Thangadurai, *ACS Appl. Mater. Interfaces*, 2020, **12**, 36119–36127.
16 A. Boulant, J. F. Bardeau, A. Jouanneaux, J. Emery, J. Y. Buzare and O. Bohnke, *Dalt. Trans.*, 2010, **39**, 3968–3975.
17 A. Sharafi, S. Yu, M. Naguib, M. Lee, C. Ma, H. M. Meyer, J. Nanda, M. Chi, D. J. Siegel and J. Sakamoto, *J. Mater. Chem. A*, 2017, **5**, 13475–13487.
18 L. Dhivya, K. Karthik, S. Ramakumar and R. Murugan, *RSC Adv.*, 2015, **5**, 96042–96051.
19 A. Sharafi, E. Kazyak, A. L. Davis, S. Yu, T. Thompson, D. J. Siegel, N. P. Dasgupta and J. Sakamoto, *Chem. Mater.*, 2017, **29**, 7961–7968.
20 Y. Li, X. Chen, A. Dolocan, Z. Cui, S. Xin, L. Xue, H. Xu, K. Park and J. B. Goodenough, *J. Am. Chem. Soc.*, 2018, **140**, 6448–6455.
21 F. Han, J. Yue, C. Chen, N. Zhao, X. Fan, Z. Ma, T. Gao, F. Wang, X. Guo and C. Wang, *Joule*, 2018, **2**, 497–508.
22 Y. Zhang, J. Meng, K. Chen, Q. Wu, X. Wu and C. Li, *ACS Appl. Mater. Interfaces*, 2020, **12**, 33729–33739.
23 M. Cai, Y. Lu, J. Su, Y. Ruan, C. Chen, B. V. R. Chowdari and Z. Wen, *ACS Appl. Mater. Interfaces*, 2019, **11**, 35030–35038.
24 P. Zhao, Y. Xiang, Y. Wen, M. Li, X. Zhu, S. Zhao, Z. Jin, H. Ming and G. Cao, *J. Eur. Ceram. Soc.*, 2018, **38**, 5454–5462.
25 K. Ishiguro, Y. Nakata, M. Matsui, I. Uechi, Y. Takeda, O. Yamamoto and N. Imanishi, *J. Electrochem. Soc.*, 2013, **160**, A1690.
26 I. McClelland, H. El-Shinawi, S. G. Booth, A. Regoutz, J. Clough, S. Altus, E. J. Cussen, P. J. Baker and S. A. Cussen, *Chem. Mater.*, 2022, **34**, 5054–5064.

27 Z. Cao, W. Wu, Y. Li, J. Zhao, W. He, J. Liu, H. Zhang and G. Li, *Ionics*, 2020, **26**, 4247–4256.
28 Y. Zhang, D. Luo, W. Luo, S. Du, Y. Deng and J. Deng, *Electrochim. Acta*, 2020, **359**, 136965.
29 H. Geng, K. Chen, D. Yi, A. Mei, M. Huang, Y. Lin and C. Nan, *Rare Met. Mater. Eng.*, 2016, **45**, 612–616.
30 Y. Meesala, Y. K. Liao, A. Jena, N. H. Yang, W. K. Pang, S. F. Hu, H. Chang, C. E. Liu, S. C. Liao, J. M. Chen, X. Guo and R. S. Liu, *J. Mater. Chem. A*, 2019, **7**, 8589–8601.
31 F. Tietz, T. Wegener, M. T. Gerhards, M. Giarola and G. Mariotto, *Solid State Ionics*, 2013, **230**, 77–82.
32 T. Thompson, J. Wolfenstine, J. L. Allen, M. Johannes, A. Huq, I. N. David and J. Sakamoto, *J. Mater. Chem. A*, 2014, **2**, 13431–13436.
33 C. Bernuy-Lopez, W. Manalastas, J. M. Lopez Del Amo, A. Aguadero, F. Aguesse and J. A. Kilner, *Chem. Mater.*, 2014, **26**, 3610–3617.
34 P. Ranque, J. Zagórski, S. Devaraj, F. Aguesse and J. M. López del Amo, *J. Mater. Chem. A*, 2021, **9**, 17812–17820.
35 G. Larraz, A. Orera, J. Sanz, I. Sobrados, V. Diez-Gómez and M. L. Sanjuán, *J. Mater. Chem. A*, 2015, **3**, 5683–5691.
36 M. Leskes, A. J. Moore, G. R. Goward and C. P. Grey, *J. Phys. Chem. C*, 2013, **117**, 26929–26939.
37 T. Liu, Z. Liu, G. Kim, J. T. Frith, N. Garcia-Araez and C. P. Grey, *Angew. Chem., Int. Ed.*, 2017, **56**, 16057–16062.
38 F. Nardelli, S. Borsacchi, L. Calucci, E. Carignani, F. Martini and M. Geppi, *Rend. Lincei Sci. Fis. Nat.*, 2020, **31**, 999–1010.
39 P. Posch, S. Lunghammer, A. Wilkening, K. Hogrefe and H. M. R. Wilkening, *JPhys Energy*, 2023, **5**, 15001.
40 A. Kuhn, M. Wilkening and P. Heitjans, *Solid State Ionics*, 2009, **180**, 302–307.
41 J. R. Hendrickson and P. J. Bray, *J. Magn. Reson.*, 1973, **9**, 341–357.
42 M. Wilkening, D. Bork, S. Indris and P. Heitjans, *Phys. Chem. Chem. Phys.*, 2002, **4**, 3246–3251.
43 J. S. Waugh and E. I. Fedin, *Sov. phys., Solid state*, 1963, **4**, 1633–1636.
44 O. Bohnke, J. Emery, A. Veron, J. L. Fourquet, J. Y. Buzare, P. Florian and D. Massiot, *Solid State Ionics*, 1998, **109**, 25–34.
45 V. Epp, Ö. Gün, H. J. Deiseroth and M. Wilkening, *J. Phys. Chem. Lett.*, 2013, **4**, 2118–2123.
46 A. Kuhn, S. Narayanan, L. Spencer, G. Goward, V. Thangadurai and M. Wilkening, *Phys. Rev. B: Condens. Matter Mater. Phys.*, 2011, **83**, 1–11.
47 O. Bohnke, J. Emery and J.-L. Fourquet, *Solid State Ionics*, 2003, **158**, 119–132.
48 M. Wilkening and P. Heitjans, *ChemPhysChem*, 2012, **13**, 53–65.
49 H. Buschmann, J. Dölle, S. Berendts, A. Kuhn, P. Bottke, M. Wilkening, P. Heitjans, A. Senyshyn, H. Ehrenberg, A. Lotnyk, V. Duppel, L. Kienle and J. Janek, *Phys. Chem. Chem. Phys.*, 2011, **13**, 19378–19392.
50 A. I. Waidha, T. Ferber, M. Donzelli, N. Hosseinpourkahvaz, V. Vanita, K. Dirnberger, S. Ludwigs, R. Hausbrand, W. Jaegermann and O. Clemens, *ACS Appl. Mater. Interfaces*, 2021, **13**, 31111–31128.
51 V. Vanita, A. I. Waidha, S. Yadav, J. J. Schneider and O. Clemens, *Int. J. Appl. Ceram. Technol.*, 2023, **20**, 236–250.